POLITECNICO DI TORINO
Repository ISTITUZIONALE

Machine learning-based automatic operational modal analysis: A structural health monitoring application to masonry arch bridges

(Article begins on next page)

29 November 2022

RESEARCH ARTICLE

Machine learning-based automatic operational modal analysis: A structural health monitoring application to masonry arch bridges

Marco Civera[1] | Vezio Mugnaini[1] | Luca Zanotti Fragonara[2]

[1]Department of Structural, Building and Geotechnical Engineering, Politecnico di Torino, Turin, Italy

[2]School of Aerospace, Transport and Manufacturing, Cranfield University, Cranfield, UK

Correspondence
Marco Civera, Department of Structural, Building and Geotechnical Engineering, Politecnico di Torino, Turin 10129, Italy.
Email: marco.civera@polito.it

Summary

Structural health monitoring (SHM) is one of the main research topics in civil, mechanical and aerospace engineering. In this regard, modal parameters and their trends over time can be used as features and indicators of damage occurrence and growth. However, for practical reasons, output-only techniques are particularly suitable for the system identification (SI) of large civil structures and infrastructures, as they do not require a controlled source of input force. In this context, these approaches are typically referred to as operational modal analysis (OMA) techniques. However, the interpretation of the OMA identifications is a labour-intensive task, which could be better automated with artificial intelligence and machine learning (ML) techniques. In particular, clustering and cluster analysis can be used to group unlabelled datasets and interpret them. In this study, a novel multi-stage clustering algorithm for automatic OMA (AOMA) is tested and validated for SHM applications—specifically, for damage detection and severity assessment—to a masonry arch bridge. The experimental case study involves a 1:2 scaled model, progressively damaged to simulate foundation scouring at the central pier.

KEYWORDS
automated operational modal analysis, damage detection, machine learning, masonry arch bridge, operational modal analysis, structural health monitoring

1 | INTRODUCTION

Structural health monitoring (SHM) is one of the fastest-growing topics among structural engineers, especially when applied in a machine learning (ML) framework.[1] This is also thanks to public opinion, which is becoming more and more sensitive to the importance of the maintenance of strategic infrastructures, the preservation of cultural heritage buildings, and the safeguarding of human life. For instance, people interact with ageing infrastructures more than ever as modernisation cannot keep up with the increasing demand for transport flows.

The constant monitoring of structures and infrastructure can give some important information about the possible damages which may arise during their service life. Moreover, an assessment of the residual life can be estimated, and

maintenance strategies may be planned in time to avoid risks to human life and structural failure which may generate damage to other buildings.

To extract useful features that characterise the behaviour of a structure or the changing of these with time, different methods of investigation can be pursued for system identification (SI).[2] The choice of the most appropriate method and the planning of study strategies depend on the typology of the object of study, the budget and many other factors.[1]

A common method is the use of vibration-based SHM, aimed at extracting useful features from the dynamic response of a structure,[3] especially in the form of modal parameters (i.e., natural frequencies, modal damping ratios and mode shapes). This is the basic concept of modal analysis, which is arguably the most common approach for SI and damage detection. When the structure can be excited with a known input, experimental modal analysis (EMA) can be applied to this aim. Several EMA approaches exist; a recent method was applied as well for masonry bridges in recent studies.[4,5] However, for massive structures and infrastructures and/or for continuous monitoring over a prolonged time, output-only methods should be preferred.

When ambient vibrations (AVs) are utilised for output-only MA, the term operational modal analysis (OMA) is used.[6] Some examples of OMA applications for large civil infrastructures can be found in the works of several authors.[7–11]

The main problem for large and complex systems is that the number of relevant modes is not known a priori. Therefore, it is not possible to guess the model order for SI. The common practice is thus to re-run the SI procedure repeatedly for an arbitrary range of model orders. The result is called a stabilisation diagram, where both physical and numerical poles (due to the overfitting of the higher order models over noisy data) are included. Thus, the actual vibrational modes need to be selected among all the identified poles, discarding the rest. This is generally performed by an expert user. Consequently, the main limitation to the extensive use of OMA for continuous monitoring is the requirement of constant supervision by a skilled professional.

This is incompatible with the need for uninterrupted structural surveillance. Therefore, the automation of the whole modal extraction procedure is a necessary step for the future generation of civil buildings; this is generally known as automatic (or automated) OMA, i.e., AOMA for short. In this regard, two extensive reviews of OMA and AOMA approaches can be found in Peeters and de Roeck and Reynders.[12,13]

A recent example of application in the ambit of continuous SHM for civil engineering is the AOMA system deployed at the Sanctuary of Regina Montis Regalis in Vicoforte, Italy.[14] Similar applications were also deployed for the famous case studies of the Z24 bridge in Switzerland[15] and the Tamar suspension bridge in Southwest England.[16] Some interesting aspects can be found in Rainieri and Fabbrocino.[17]

Very recently, Cheema et al.[18] applied a Dirichlet process Gaussian mixture model (DP-GMM) clustering approach to discern true physical modes from the mathematically spurious modes on a cable-stayed bridge in New South Wales, Australia. He et al.[19] applied a modified version of fuzzy C-means (FCM) clustering to the Fourth Nanjing Yangtze River Bridge. Zeng and Hoon Kim[20] tested a self-adaptive clustering approach with a weighted multi-term distance on the Z24 and Downing Hall benchmarks. The classic hierarchical clustering-based AOMA was applied by Anastasopoulos et al.[21] to almost one year of acquisitions from a steel single-span tied arch railway bridge. Indeed, the Structural Mechanics Section of KU Leuven developed a MatLab® Toolbox,[22] which, similarly to the algorithm applied here for this study, includes (among some other options) an SSI algorithm.[23] The method was tested on footbridges[24] and other steel, concrete or even composite infrastructures (e.g., Reynders et al. and Liu et al.[25,26]).

Among all the large civil constructions, bridges are arguably the ones of major interest, for several reasons. The main factor derives from their strategic importance as the commercial arteries of any country. They also pose a potentially serious threat to human lives due to the intense traffic which they sustain daily. Some recent events, for instance, are well-descriptive of the risks of bridge structural failures. The collapse of the Morandi Bridge in Genoa on 14 August 2018 caused tens of victims, hundreds of displaced inhabitants and millions of euros of direct economic losses, even without considering the long-term socio-economic consequences of the disruptions. On a smaller scale, these were the same aftermaths faced after the 19th April 2017 viaduct collapse in Fossano (Piedmont), the 9th March 2017 viaduct collapse in Camerano (Marche), the 23rd January 2017 event of Fiumara Allaro (Calabria), the 28th October 2016 event of Annone and the very recent collapse of the bridge of Albiano Magra (Tuscany) happened the 8th April 2020, just to cite some of the most recent bridge and viaduct failures in Italy.

This is even more accentuated for historical bridges, as they do not only have an economic and practical value but also an architectural and cultural one. More specifically, masonry structures are notoriously difficult to handle, model[27] and investigate.[28] Their dynamic response is also very sensitive to damage.[29] All these aspects are mainly due to the

uncertainties and complex interactions which are characteristic of their building materials.[30] The natural ageing of these materials (with most of the cultural heritage being centuries-old) can only aggravate the situation. In this regard, the non-destructive testing (NDT) and the continuous monitoring of existing masonry arch bridges are a complex yet necessary requirement. An investigation about a recent and interesting case of scour-induced collapse for a multi-span masonry arch bridge can be found in Scozzes et al.[31] Two examples concerning railway masonry bridges are reported in Costa et al.[32,33]

All the previous studies reported in the scientific literature point out the effectiveness and efficiency of OMA and AOMA for the SHM of bridges of any size and use,[34–36] ranging from long-span cable-stayed bridges[37] to iron arch ones[38] and pedestrian walkways.[39] However, to the best of the authors' knowledge, there is still a lack of AOMA applications to masonry arch bridges in the scientific literature to this day.

The procedure described here is characterised by a novel approach for discerning the physical modes from the computational ones. This overcomes the current issue of spurious modes, which can affect the results. In the scenario investigated in Politecnico di Torino's laboratories, the scouring of the central pile was emulated by means of imposed foundation settlements and rotations; further detail will be provided in the next sections.

The rest of this paper is organised as follows. Section 2 briefly discusses the AOMA procedure. Section 3 describes the case study, i.e., the 1:2 scaled model of the masonry two-span arch bridge. Section 4 reports the results, and the paper ends with the Conclusions.

2 | THE AOMA PROCEDURE

The algorithm applied and tested here for SHM purposes consists of the preliminary application of the stochastic subspace identification (SSI) algorithm, followed by four consecutive steps:

1. application of SSI for an arbitrary range of model orders;
2. a preliminary partition by hard validation criteria (HVC);
3. a further selection by soft validation criteria (SVC);
4. the cluster-based modal identification; and
5. the modal parameters identification.

After the initial identification of the poles, the four-stepped concept follows closely the classic procedure defined by Reynders and colleagues[40]; this is intended for the cleansing of the stabilisation diagram. The main aspects are here recalled for completeness.

The HVC are physically based and enforce commonsense rules. The SVC, on the other hand, are purely data driven and do not rely on any further assumptions. In this aspect, clustering and cluster analysis, which are important ML techniques, can be used. The concept is to binary classify the remaining poles as stable or unstable and discard the latter ones, while the elements of the first group are passed to the next phases.

The same ML approaches can be applied for the following steps as well. In the clustering phase, the poles that passed both HVC and SVC selections are grouped together according to their distances. These clusters are then further sifted: The ones classified as 'most probably physical' are considered as representing a distinct vibrational mode, while the others (assumed as certainly numerical) are discarded. Finally, in the last step, the modal parameters which best characterise any remaining cluster (i.e., its natural frequency, damping ratio, and mode shape) are statistically defined, based on the poles included in it.

The four steps can be further detailed as reported in the following subsections.

2.1 | Hard validation criteria

Three rules are implemented for the HVC. These reflect the suggestions made by Reynders et al.[13,40] The poles with negative or excessively high damping ratios are immediately discarded as unrealistic. The higher boundary is set to 20% according to Cabboi et al. and Demarie and Sabia.[38,41] Real-valued poles are rejected as well since a zeroed imaginary part would mean a non-vibrational free decay, which is certainly spurious for an oscillatory response.

2.2 | Soft validation criteria

Five parameters are considered for the definition of the SVC: the eigenvalues λ, the natural frequencies f, the damping ratios ξ, the complementary of the modal assurance criterion $\nu = 1 - MAC$, and the mean phase deviation MPD. These will be described in more detail later on. For each one of these parameters, the absolute differences between the poles for different model orders are computed. These are then utilised to define if the pole is stable or not. The rationale for preferring absolute differences over the more traditional approach (relative differences) was investigated and described in previous works.[42]

In this discussion, the model order is defined accordingly to the number of corresponding poles. Since poles are complex conjugated, the model order ranges between the (arbitrarily defined) n_{min} and n_{max} with increments of two ($n_{min}, n_{min} + 2, n_{min} + 4, ..., n_{max}$). $l_n(n) = n - n_{min}$ indicates the number of poles belonging to the nth model order. Therefore, the comparison parameters are defined for any $i = 1, 2, ..., l_n$ pole belonging to the model order n when coupled to any $m = 1, 2, ..., l_{n+2}$ pole belonging to the next model order $n + 2$. For a generic parameter p, that means

$$\Delta \boldsymbol{p^n}_i : \Delta p^n_{i,m} = \left| p^n_i - p^{n+2}_m \right|, \tag{1}$$

where $\Delta \boldsymbol{p^n}_i$ denotes the array of absolute differences for the ith pole of the nth model order, while $\Delta p^n_{i,m}$ is its mth term. Equation (1) can be rewritten to accommodate $p = \lambda, f, \xi, 1 - MAC$, or MPD, considering that $\Delta \boldsymbol{\lambda^n}_i \in \mathbb{C}^{1 \times l_{n+2}}$ for the complex-valued eigenvalues, while the arrays of the other parameters are subsets of $\mathbb{R}^{1 \times l_{n+2}}$.

The modal assurance criterion (MAC) is computed between the mode shapes $\boldsymbol{\phi}_i^n$ and $\boldsymbol{\phi}_m^{n+2}$ according to its classic definition[43]

$$MAC\left(\boldsymbol{\phi}_i^n, \boldsymbol{\phi}_m^{n+2}\right) = \frac{\left[(\boldsymbol{\phi}_i^n)^* (\boldsymbol{\phi}_m^{n+2}) \right]^2}{\left[(\boldsymbol{\phi}_i^n)^* (\boldsymbol{\phi}_i^n) \right] \cdot \left[(\boldsymbol{\phi}_m^{n+2})^* (\boldsymbol{\phi}_m^{n+2}) \right]}, \tag{2}$$

while MPD is defined as in Philips and Allemang.[44] In conclusion, these comparison parameters form a five-dimensional (5D) space, where the poles can be clustered.

To do so, once these five arrays have been defined, the distance between poles of subsequent model orders is evaluated as

$$\boldsymbol{d}_i^n = \boldsymbol{\Delta f}^* + \boldsymbol{\nu}^*, \ \boldsymbol{d}_i^n \in \mathbb{R}^{1 \times l_{n+2}}, \tag{3}$$

with the first term computed as in Equation (1) (for $\Delta \boldsymbol{p} = \Delta \boldsymbol{f}$) and then min-max normalised, that is to say,

$$\boldsymbol{\Delta f}^* = \frac{\Delta \boldsymbol{f^n}_i - min(\Delta \boldsymbol{f^n}_i)}{max(\Delta \boldsymbol{f^n}_i) - min(\Delta \boldsymbol{f^n}_i)}. \tag{4}$$

Such that $\Delta \boldsymbol{f}^*$ is defined between 0 and 1 and thus comparable with $\boldsymbol{\nu}^* \equiv \boldsymbol{\nu}_i^n$ (in both cases, zero corresponds to no correlation, and maximum similarity tends to 1). Please note that Equation (3) is similar yet different to the classic procedure described in Reynders et al.,[13] where the (min-max normalised) eigenvalue distance in the complex plane $\Delta \lambda$ is utilised in lieu of the (min-max normalised) difference of eigenfrequencies $\Delta \boldsymbol{f}$. The rationale for this design choice implemented here was to not include the dependence on the damping estimates, which are well-known to be less reliable and subject to greater variability than frequency and mode shape estimates.[45]

At this point, for the ith pole of the nth model order, the 'neighbouring pole' is defined as the single pole belonging to model order $n + 2$ corresponding to the minimum value of $\boldsymbol{d}_i^n$, i.e.

$$\Delta p_i^n = \Delta \boldsymbol{p}_i^n \left(arg \, min \left(\boldsymbol{d}_i^n \right) \right). \tag{5}$$

Therefore, five scalars are extracted from the five arrays $\Delta \boldsymbol{p^n}_i$. This process is reiterated for all the poles belonging to a model order and then to all model orders. The resulting values are then concatenated (for any of the five parameters) into a unique vector $\Delta \boldsymbol{p}$, defined as

$$\Delta \boldsymbol{p} = \left[\Delta \boldsymbol{p^{n_{min}}} \Delta \boldsymbol{p^{n_{min}+2}} \Delta \boldsymbol{p^{n_{min}+4}} ... \Delta \boldsymbol{p^{n_{max}-2}} \right]^T, \tag{6}$$

where for any model order

$$\Delta \boldsymbol{p^n} = \left[\Delta p_1^n \Delta p_2^n ... \Delta p_{l_n(n)}^n \right]^T, \tag{7}$$

with Δp_1^n, Δp_2^n, ...$\Delta p_{l_n(n)}^n$ defined as for Equation (5).

Remembering that $\Delta \boldsymbol{p}$ is intended here as a shorthand for $\boldsymbol{\Delta \lambda}$, $\boldsymbol{\Delta f}$, $\boldsymbol{\Delta \xi}$, $\boldsymbol{\nu}$, or $\boldsymbol{\Delta MPD}$, the stable and unstable poles will be defined through k-means clustering (with $k=2$) in the 5D space defined by the comparison parameters, according to their distance. However, before doing so, another intermediate step is required.

The clustering algorithm assumes a Gaussian distribution of these parameters.[46] Since this may be not satisfied by the raw parameters (as highlighted by Neu et al.[47]), a Box–Cox transformation is applied to each one of the five arrays $\boldsymbol{\Delta p} = \boldsymbol{\Delta \lambda}$, $\boldsymbol{\Delta f}$, $\boldsymbol{\Delta \xi}$, $\boldsymbol{\nu}$, $\boldsymbol{\Delta MPD}$, as

$$\boldsymbol{h}(\gamma) = \begin{cases} (\boldsymbol{\Delta p} - 1)/\gamma, & \gamma \neq 0 \\ \ln \boldsymbol{\Delta p}, & \gamma = 0 \end{cases} \tag{8}$$

where the transformation parameter γ is defined through profile log-likelihood maximisation as described in the original paper of Box and Cox.[48] At this point, the z scores of the obtained $\boldsymbol{h}$ arrays are computed, separately for the five cases, as

$$z_i^n = \frac{h_i^n - \mu_p}{\sigma_p}, \tag{9}$$

where μ_p is the global mean and σ_p the global standard deviation, respectively computed as

$$\mu_p = \frac{1}{L} \sum_{n \in N} \sum_{i=1}^{l_n} h_i^n, \tag{10}$$

and

$$\sigma_p = \sqrt{\frac{1}{L} \sum_{n \in N} \sum_{i=1}^{l_n} \left(h_i^n - \mu_p \right)^2}, \tag{11}$$

where $N = [n_{min}, n_{min+2}, n_{min+4}, ..., n_{max}]$ is the array of the considered model orders. Note that the length of the resulting $\boldsymbol{z}$ array is equal to $L = \sum_{n \in N} l_n(n)$. At this point, is finally possible to define the two clusters—stable and unstable poles—in the 5D space defined by the z scores of the Box–Cox transforms of the five $\boldsymbol{\Delta p}$ arrays.

2.3 | Cluster-based modal identification

In this third step, the poles are firstly clustered according to their distances and by means of hierarchical clustering. Then, the obtained clusters are in turn divided between physical and non-physical (computational) modes. Finally, for any remaining cluster, the poles flagged as outliers are removed.

2.3.1 | Hierarchical clustering

At this point, the vector d_i^n described in Equation (3) is extended to include all model orders, resulting in the L-by-L distance matrix D, the generic term of which can be defined (for the uth row and vth column) as

$$D_{u,v} = \frac{\Delta f_{u,v} - min(\Delta f_{u,v})}{max(\Delta f_{u,v}) - min(\Delta f_{u,v})} + \nu_{u,v}, \tag{12}$$

considering

$$\Delta f_{u,v} = |f_u - f_v|, \ \nu_{u,v} = 1 - MAC(\phi_u, \phi_v). \tag{13}$$

The symmetry of the square matrix D is exploited by considering only its lower triangular part. Moreover, the distances among the poles belonging to the same model order are not considered. This reflects the fact that, by definition, two poles from the same identification cannot represent the same mode. This is intended to manage pole splitting at high model orders, as evidenced in Mugnaini et al.,[42] Section 2.6. Thus, $D_{u,v} = $ NaN was forcefully imposed in these cases.

The terms in D are then used to hierarchically cluster the poles according to their neighbourhood. The agglomerative (bottom-up) process is stopped when the inter-cluster distance, defined with the average linkage method[49] as

$$\ell(q,t) = \frac{1}{n_q n_t} \sum_{i=1}^{n_q} \sum_{j=1}^{n_t} D(u = x_{qi}, v = x_{tj}) \tag{14}$$

reaches a threshold value $\widetilde{d}$, defined according to the algorithm detailed in Neu et al.[47] It is worth mentioning that Reynders et al.[40] proposed a stricter threshold definition; however, this alternative was tested here as well and found to be almost inconsequential.

In Equation (14), x_{qi} and x_{tj} indicate the ith and jth elements of the two clusters q and t, where n_q and n_t are the number of elements included in these two groups. The algorithm of the hierarchical clustering described in Algorithm 6.4.1 from Aggarwal[50] was only slightly modified to account for the presence of the NaN terms. The complete implementation is reported in detail in Mugnaini et al.[42] (Algorithm 1) and is here omitted for brevity.

2.3.2 | Selection of physical clusters

This step represents the main novelty (even if not the only one) with respect to the similar, already-existing AOMA procedures such as the ones of Reynders et al.[40] and Neu et al.[47] As in these two well-known procedures, the clusters are labelled as 'possibly physical' (PP) or 'certainly mathematical' (CM) according to the number of poles included. The rationale is that clusters with very few poles are almost surely computational. However, in all classic implementations, this is performed (again) through 2-means clustering.[40] This approach is understandable since it is intended to distinguish between only two categories—CM and PP. However, the use of the adjective *possibly* physical in Reynders et al.[40] (and *probably* physical in Neu et al.[47]) implicitly states that the use of 2-means clustering is largely conservative, in the sense that it tends to preserve non-physical modes rather than risking to discard actual ones. On the one hand, this unbalance makes practical sense since the risk of missing a weakly excited mode is far more consequential than the outcomes of retaining a few spurious identifications. However, on the other hand, this was found to be excessively unbalanced, often leaving too many mathematical modes to be discarded in the next subsequent step or by user manual selection. This was found as well in previous numerical and experimental applications,[42] which motivated this research for a stricter sifting strategy.

To bypass this problem, a tuneable method is here proposed. This can be seen as a variation of the previous technique. The procedure is as follows:

1. To improve the stability of the process, a number w of empty clusters is artificially added (with w corresponding to 20% of the number of poles included in the largest cluster, as suggested by Reynders et al.[40])
2. The k-means clustering is performed, with $k = 2$, to obtain the two CM and PP centroids.
3. For any potential mode, the distances from the CM and PP centroids are calculated as DI_{CM} and DI_{PP}.
4. The total index is computed as $DI_{TOT} = \left(\frac{DI_{CM}}{max(DI_{CM})} + \left(1 - \frac{DI_{PP}}{max(DI_{PP})} \right) \right) / 2$.
5. For any candidate mode, the percentage $DI_\%$ is obtained as $DI_\% = \frac{DI_{TOT}}{max(DI_{TOT})} \cdot 100$.

At this point, $DI_\%$ can be seen as a *probability of physical meaningfulness*. The upper limit (100%) is set by the point(s) closer to the PP centroid and farther from the CM one and thus certainly physical. The user can then manually set the threshold of probability as desired. It derives from the classic implementation of the k-means clustering that for $k = 2$, the threshold is implicitly set to 50%. The proposed variant allows selecting a different value to require a stricter selection of physical modes, discarding the other (less probably physical) ones.

Regarding Step (1), the addition of the empty clusters did not produce any noticeable improvement, at least for the case study here inspected. The resulting modes did not change significantly even by adding empty clusters as suggested by Reynders et al.[40] However, this can be a specific aspect of the case analysed, and no detrimental effects were caused by it. Therefore, the 20% value suggested in the literature was kept in use.

After these, only the physically meaningful clusters are passed to the next step.

2.3.3 | Outlier removal

An outlier detection procedure is run on the remaining clusters. Specifically, the mean absolute deviation (MAD)[51] is calculated among the poles belonging to the same group. The poles that have at least one among Δf, $\Delta \xi$, or ν higher than 3 scaled MAD from the cluster median are removed. The remaining poles are used to characterise the modal parameters of their corresponding cluster in the next step.

2.4 | Identification of the modal parameters

Four statistical measures were investigated to better define the cluster-wide parameters. These four options were found to be equivalent with no major differences in the results. These methods can be briefly described as follows:

1. Method 1: Assigning to each cluster the mean of frequency, damping ratio, and (normalised) mode shape ($\overline{f}$, $\overline{\xi}$, and $\overline{\phi}$, in this order).
2. Method 2: Assigning to each cluster the modal parameters of the pole which minimise the distance between the mean of the damping ratios $\overline{\xi}$ and its own ξ.
3. Method 3: Assigning to each cluster the modal parameters of the pole which minimise the sum of the three distances $\overline{f} - f$, $\overline{\xi} - \xi$, and $\overline{\phi} - \phi$.
4. Method 4: Assigning to each cluster the modal parameters of the pole which minimise $\overline{\phi} - \phi$.

Having defined the whole AOMA procedure, the shifts in frequency and the other modal parameters can be directly linked to the developing damage, as this induced a stiffness reduction in the monitored system. This is here validated on the 1:2 scale model of the masonry arch bridge.

3 | THE MASONRY TWO-SPAN ARCH BRIDGE

The test structure is not an exact reproduction of an existing bridge but was purposely designed taking into account common features, geometric proportion, and historical design codes. The intent was to recreate the main characteristics of Italian masonry arch bridges.

3.1 | The experimental setup

The model (portrayed in Figure 1a) was built with clay bricks sized according to the adapted scale law (130 × 65 × 30 mm). The geometry of the two-span arch bridge is described in Table 1; its mechanical properties (Young's modulus E, Poisson ratio ν, and the S and P wave velocities V_s and V_p) are reported in Table 2. Construction materials (bricks and mortar) with poor mechanical resistances were purposely chosen to be similar to the aged materials of historical buildings.[52] The arch barrels were stabilised with a backfill made up of a mix of gravel, sand, and debris, topped by a levelled 10 cm-thick concrete layer. The whole structure rested on two reinforced concrete slabs, fixed to the floor. Further details can be found in Ruocci et al.[52,53]

A settlement application system was inserted under the central pile to investigate the effect of the displacements and rotations imposed at the masonry pier. These were intended to emulate riverbank erosion and calibrated accordingly to ad hoc hydraulic flume tests.[53] A thin layer of polystyrene, set in between the top steel plate of the settlement
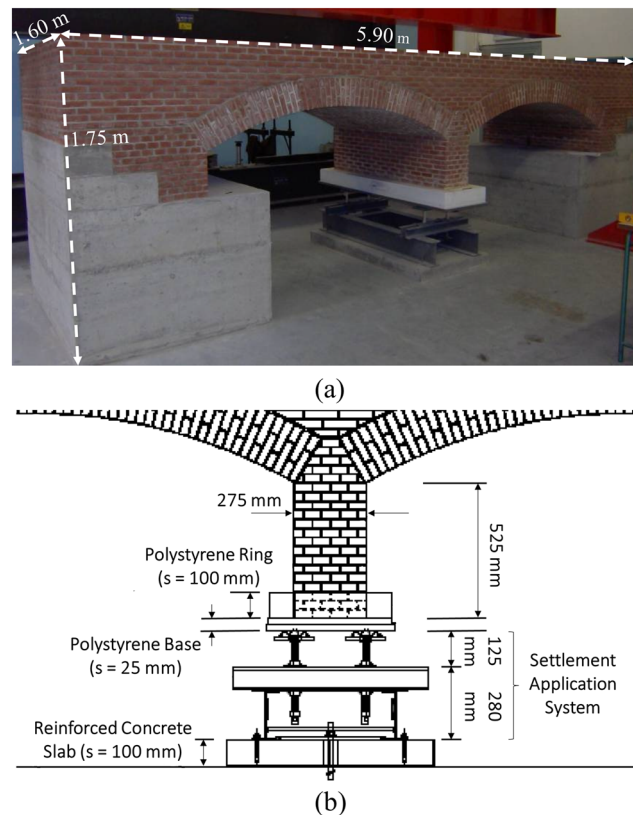
FIGURE 1 (a) Photo portrait of the 1:2 scaled bridge model. (b) The settlement application system, front view (adapted from Ruocci et al.[53,54])

TABLE 1 Geometry of the bridge model

Parameter	Value	Measurement unit
Total width	1.55	m
Total height	1.73	m
Total length	5.87	m
Arch span	2.00	m
Arch radius	2.00	m
Arch angular opening	30	°

Note: Values were retrieved from Ruocci.[53]

TABLE 2 Construction materials

Material	E (MPa)	ν (−)	ρ (kg/m³)	V_p (m/s)	V_s (m/s)
Masonry	1500	0.20	1900	937	574
Backfill material	50	0.10	2000	160	107
Concrete	5000	0.15	2200	1549	994
Reinforced concrete	30,000	0.15	2400	3633	2331

Note: Values were retrieved from Ruocci.[53]

TABLE 3 Experimental campaigns

	Damage step	Time	Settlement at the central pier (mm)	Rotation at the central pier (rad)	Polystyrene removed (%)
First exp. campaign	Healthy state (HS)	April 2009	0	0	0%
	DS1	//	0	0	18.0%
	DS2	//	0.25	0	25.0%
	DS3	//	1.00	$4.21\ 10^{-4}$	37.5%
	DS4	//	2.25	$1.01\ 10^{-3}$	47.0%
Second exp. campaign	DS5 (post-relaxation)	September 2010	2.25	$1.23\ 10^{-3}$	56.0%
	DS6	October 2010	2.80	$1.23\ 10^{-3}$	72.0%
	DS7	//	3.60	$1.27\ 10^{-3}$	81.0%
	DS8	//	4.70	$1.30\ 10^{-3}$	91.0%
	DS9	//	7.60	$1.28\ 10^{-3}$	100.0%

application system and the bottom of the mid-length pier, simulated the riverbed sediment. This was progressively taken off to simulate the progressive erosion. Special attention was dedicated to replicating in situ effects; all details can be found in Civera et al. and Ruocci.[5,53]

3.2 | Damage scenarios

An increasing amount of damage was induced by applying controlled displacements and rotations at the central pier and by progressively removing the 100-mm-thick polystyrene ring layer that surrounded the pier (as shown in Figure 1b). The rotations were set to simulate natural scouring conditions, according to the procedure and assumptions detailed in Ruocci[53] (Section 9.2) and Civera et al.[5] (Section 5.1.1), arbitrarily considering one flank of the bridge to represent the upstream side.

The tests were performed in two separate experimental campaigns, following the consecutive damage steps (DSs) detailed in Table 3. After the end of the last DS (DS9), the central pier was further let settle at around 10.9 mm with all the polystyrene being removed and for the same rotation as in the last step.

Two sensor layouts, named Setups #1 and #2, were used for each DS. Their disposition was set as discussed in Ruocci[53] (Sections 6.1.2 and 10.2.2) and portrayed in Figure 2. These layouts were selected according to practical concerns, which considered as well the results from some optimal sensor placement (OSP) algorithms, specifically the effective independence, the eigenvalue vector product and other methods. These and other classic algorithms are described in more detail with an example of masonry structures in Civera et al.[29] Eighteen monoaxial PCB Piezotronics accelerometers were utilised in both configurations. Each sensor had a sensitivity of 1 V/g, a measurement range of ±3 g, and a resolution of 30 μg, for a weight of 17.5 g and a sampling frequency f_s of 400 Hz. The AV tests were performed by recording the output-only structural behaviour for 180 s. The two-span masonry arch bridge was investigated
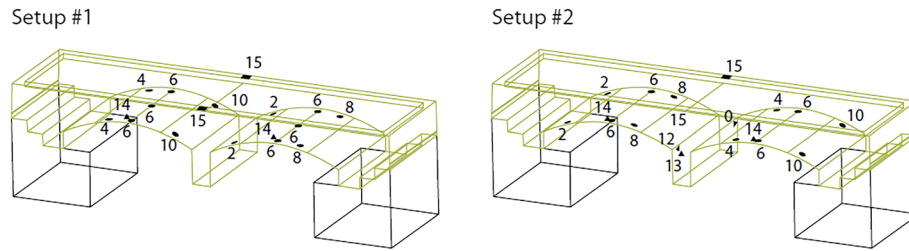
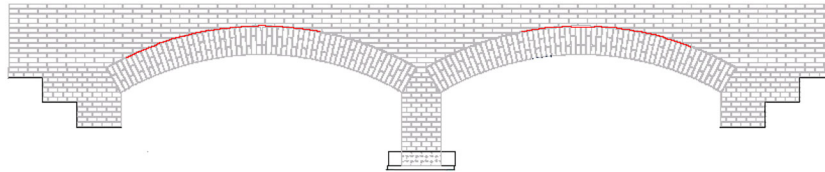**FIGURE 2** Sensor Setup #1 and #2. Adapted from Ruocci et al.[52]

FIGURE 3 Cracks detected on the external masonry surface (upstream side) due to the applied rotations and settlements. Adapted from Ruocci[53]

as well by means of input–output approaches via hammer and shaker harmonic tests, as reported in other studies (e.g., Civera et al. and Zanotti Fragonara et al.[5,55]).

Due to both the material non-linearities and the developing cracks, the structural response was affected by the presence of strong non-linear distortions (a complete discussion about the non-linear characterisation of the structure is reported in Zanotti Fragonara et al.[55]). However, these noise-like effects did not undermine the AOMA procedure, which proven to be robust to non-linearities and measurement noise. The effects of the simulated scouring on the modal parameters of the target structure were linked to the cracks developing after the application of the settlements, as already noticed in Ruocci et al.[54] These cracks are represented by the thick red lines in Figure 3; they were mostly encountered on the upstream side at the interface between the arches and the spandrel and on the arch barrels themselves.

4 | RESULTS

4.1 | SSI identification: Range of model orders and Hankel matrix

Before moving to the results of the case study, it is necessary to define how the SSI parameters have been set. The dimension of the Hankel matrix for OMA depends on the range of model orders considered in the process. Specifically, it consists of i block rows and j block columns, where this latter parameter is generally assumed as a dependent variable. That is to say, van Overschee and de Moor[56] suggested using the empirical relations

$$j = s - 2i + 1, \tag{15}$$

where s indicates the number of available measurements and i is defined as

$$i = int\left(2\frac{n_{max}}{n_{ch}}\right), \tag{16}$$

where n_{ch} is the number of output channels. The function $int()$ means the integer part. However, this is not the only option for the definition of the block rows of the Hankel matrix. Another common formulation, which is independent of the number of channels and the maximum order but dependent on the sampling frequency, is

$$i \geq \frac{f_s}{2f_0}. \tag{17}$$

Both Equations (16) and (17) were found to be unfitted for the specific case study described here. Specifically, Equation (16) returned an underestimated value of i, while Equation (17) returned an arguably excessive dimension. This did not negatively affect the results but it might cause an unnecessary computational burden since the computational requirement increases proportionally to i^2 (van Overschee and de Moor,[56] Appendix B.2.1). For this reason, the formulation

$$i = int\left(6\frac{n_{max}}{n_{ch}}\right) \tag{18}$$

will be used. While being more cautionary than Equation (16), Equation (18) does not increase the computational need to the same level as Equation (17). Moreover, the AOMA algorithm was found to work well with the range of model orders defined as follows:

- n_{min} at least as high as the number of the degrees of freedom (DoFs) of the structure, if known, or of the DoFs of interest, otherwise (this lower bound can be nevertheless increased at will);
- n_{max} at least four times the number of DoFs of interest and guaranteeing at least 25 model orders in each analysis.

This aspect will be further discussed at the end of this section.

4.2 | Results of the automatic OMA procedure

For brevity, only the analysis of a single acquisition for the healthy state (HS) with Setup #1 is here discussed in detail, for illustrative purposes only. The same steps were applied to the other acquisitions and damage scenarios, returning similar intermediate results. The overall aim was to define at least the first four modes of the structure, which were deemed as the most important ones. These correspond to the first vertical bending, the first longitudinal bending, the first lateral bending, and the first torsional mode, in this order. They were all expected to be found in the 0–50 Hz range. The range of model orders was set between $n_{min} = 40$ and $n_{max} = 90$, i.e. with n_{min} and n_{max} larger than the minimum values as defined in the previous Section 4.1 and distanced by 25 orders as deemed necessary. The Hankel matrix was dimensioned according to Equation (18).

Out of all the identified poles, 154 of them were discarded after the preliminary partition by HVC (the vast majority because of the damping ratio exceeding the higher bound at 20%). Were further reduced to 345 after SVC. These corresponded to the modes deemed as stable, accordingly to the following data-driven thresholds (Table 4):

The distribution of poles satisfying these requirements is depicted in Figure 4. As it can be seen from Figure 4b, 87% of the poles deemed as stable presented a value Δf less than or equal to 0.1 Hz. The stability of the other comparison parameters is even better, with 97% of the poles having a value of (1-MAC) lower than 0.05.

TABLE 4 Data-driven thresholds for the soft validation criteria

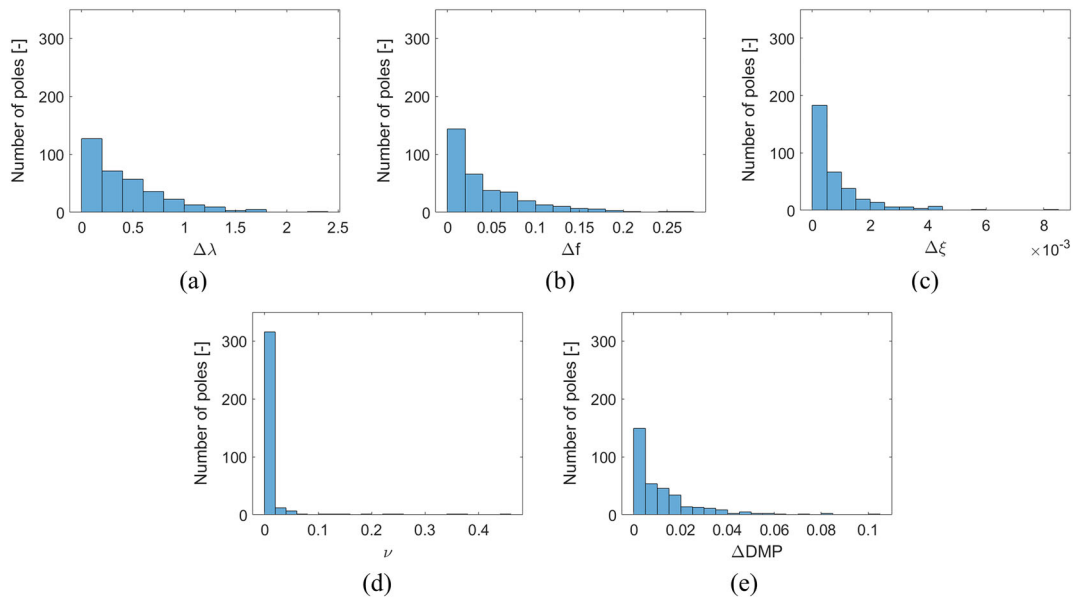| Comparison parameter	Maximum value allowed for stable poles
$\|\Delta\lambda\|$	2.375 [−]
Δf	0.262 Hz
$\Delta\xi$	0.83%
ν	0.447 [−]
ΔMPD	0.100 [−]

FIGURE 4 Distribution of the comparison parameters: Difference of eigenvalue (a), difference of frequency (b), difference of damping ratio (c), 1-MAC (d), and difference of MPD (e)
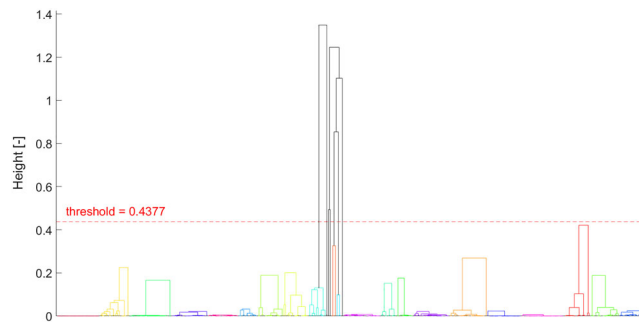

FIGURE 5 Dendrogram for HS. The dotted red line represents the cut-off corresponding to the data-driven threshold. Each cluster below the threshold was accounted as representative of a single mode, indicated by a different colour.

The resulting 25 clusters, shown by the dendrogram in Figure 5, were found for a threshold of $\widetilde{d} = 0.4377$, obtained from the fitting depicted in Figure 6a. The distribution follows the Weibull distribution for the majority of its data. The quality of the clustering can be appreciated by the Silhouette profile[57] reported in Figure 6b.

At this point, the selection of the physical clusters was initially performed via the classic approach, i.e., through 2-means clustering. As a result, any cluster with nine or more poles inside was labelled as a 'PP' mode. Eight clusters satisfied this further requirement in the 0–50 Hz range; they are portrayed in the top row of Figure 7. However, from a comparison with the reference benchmark (Ruocci,[53] Section 10.4), it was found that some modes (enclosed in red frames in Figure 7a,b) were not physical. Remembering that the 2-means clustering corresponds to a 50% probability of being physically meaningful (accordingly to the definition proposed in Section 2.3.2), it is evident that this value is not optimal; the last accepted mode has $DI_\% = 51.96\%$ while the first one rejected has $DI_\% = 47.79\%$. The difference between these two is too small to be significant.

According to this reasoning, the threshold was raised to include only modes with an 80% probability. This stricter requirement was found to correspond to at least 14 poles per cluster, resulting in the diagrams of Figure 7c,d. This new set of results matches well the expectations.

Finally, the outliers were removed from within each one of the five clusters encountered in the range of interest (0–50 Hz), accordingly to the procedure described in Section 2.3.3. The resulting modal damping ratios and natural frequencies were estimated according to the procedure described in Section 2.4; the results are reported in Table 5. These correspond to the mode shapes portrayed in Figure 8. For comparability, the MAC values between the identified mode
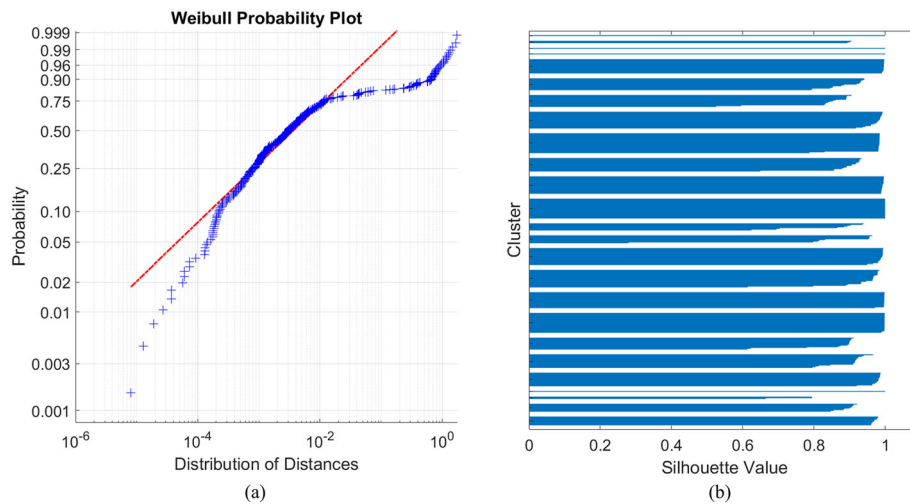
FIGURE 6 (a) Weibull fitting for thresholding; (b) silhouette profile for HS

shapes and the known targets are reported in Table 6. Regarding the first four modes, these were found to be overall consistent with the estimates reported in the previous works from Ruocci and co-authors.[52–54] The second lateral bending mode was also encountered here, very close to the upper limit of the investigated frequency range. The estimated damping for this latter mode diverges significantly from the expected value; however, as it will be shown later, this was due to the specific sensor layout. The second setup returned more realistic results.

4.2.1 | Identified shifts in the modal parameters

The modal parameters were then extracted from the subsequent recordings, to track their changes for an increasing amount of damage. Figure 9 describes these trends for the first four natural frequencies. Please note that for the first mode, the values of the first two steps (19.14 and 19.22 Hz, respectively) are too close to be clearly distinguishable in the plot. Again, it was found an overall good agreement with the results reported in Ruocci et al.[52] It is important to remark that in Ruocci et al.,[52] the estimated frequencies were obtained by averaging several acquisitions, taken from both hammer and AV tests, performed with the two sensor setups and at different moments.[53] Instead, the results for the AOMA procedure reported in Figure 9 are derived from a subset of those acquisitions, considering only AV tests, with three recordings per case and per sensor setup.

The resulting frequency shifts of the first four vibrational modes follow the same behaviour observed and described in Ruocci et al.[52,53] They can offer some useful insights into the structural changes undergone by the masonry bridge.

During the 2009 campaign, a monotonic decrease was observed, due to the global stiffness degradation (mainly localised in the central pier because of the changing boundary conditions). The slight increase of the first natural frequency between HS and DS1 was due to the concurrent addition of masses located at the central pier to mimic the weight of the lower half of the same.[53] In between the 2009 and the 2010 campaign, the central pier, which was almost suspended at the end of DS4, had the time to settle and recover some boundary stiffness in the vertical direction. This induced a counterintuitive and unexpected increase of the first natural frequency (linked to the vertical bending) despite the induced rotation and the removed material in DS5. This recovery was almost immediately lost with the application of the further DSs. All these aspects were documented in Ruocci[53] and found in these studies as well.

For context, the effects of damage-unrelated confounding influences, especially environmental and operational variations (EOVs[58,59]), are one open challenges for frequency-based damage detection (FBDD). For instance, without proper compensation and/or data normalisation, temperature-induced softening or hardening (in warmer/colder conditions, respectively) can easily exceed, e.g., crack-induced effects, causing false alarms or masking the development of damage.[60] This applies to all building materials, yet it is even more relevant for masonry structures due to their specific temperature-dependent behaviour, which makes them harder to accurately predict[61] and highly influenced by seasonal trends in temperature.[62] For the case study of the masonry arch bridge investigated here, these thermal effects were investigated in Ruocci,[53] Chapter 6.4.
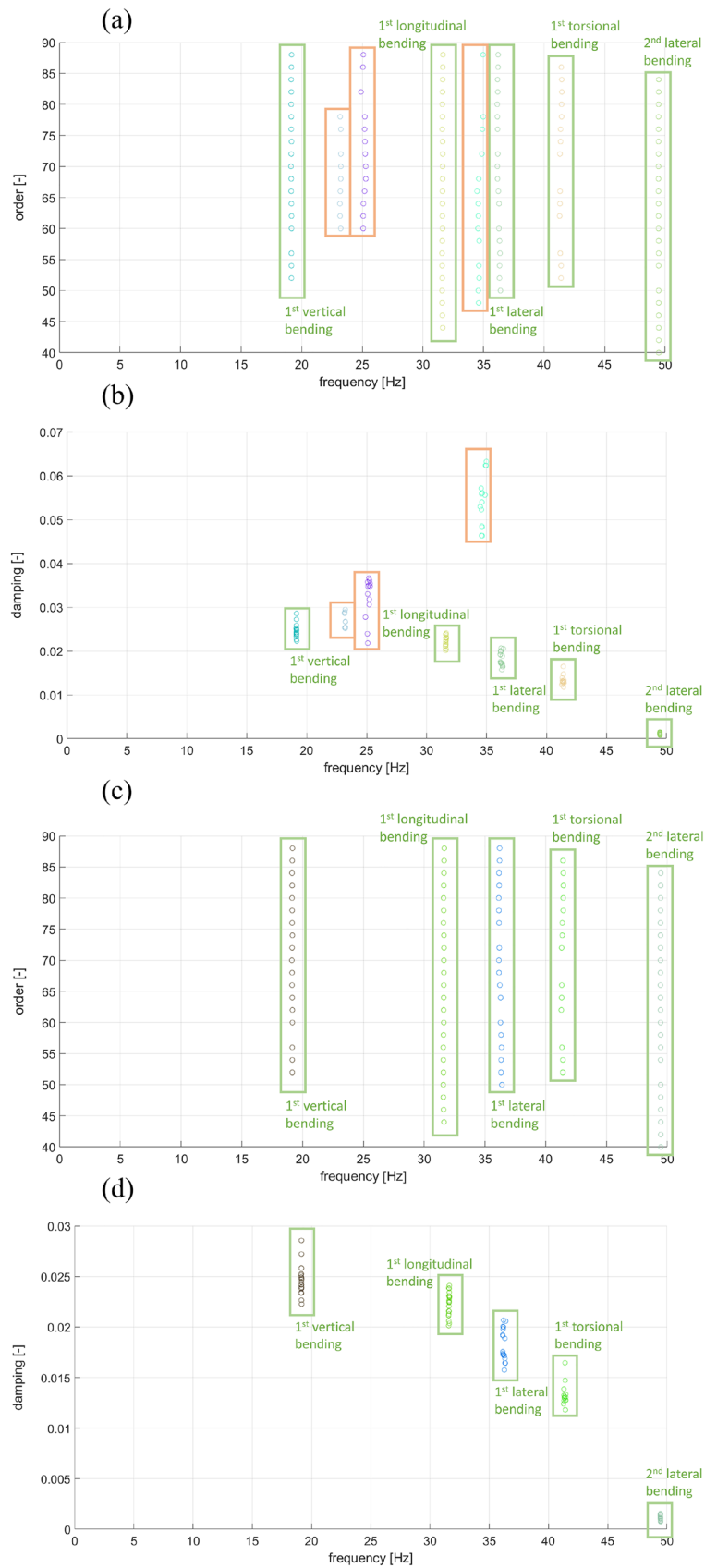
FIGURE 7 Cleaned stabilisation diagrams (HS). (a and b) Mode selection by 2-means clustering. (c and d) Mode selection with the proposed variant (acceptance threshold: 80%). The modes consistent with Ruocci[53] are enclosed by a green frame; the inconsistent ones by a red frame.

T A B L E 5 Identified modal parameters

| Mode | AOMA procedure (healthy state) | | Benchmark (Ruocci,[53] Section 10.4) | |
	Natural frequency (Hz)	Damping ratio (%)	Natural frequency (Hz)	Damping ratio (%)
I	19.14	2.5	18.94	5.5
II	31.61	2.2	30.65	3.1
III	36.23	1.8	36.23	3.6
IV	41.38	1.3	40.93	2.5
V	49.45	0.1	51.95	5.1
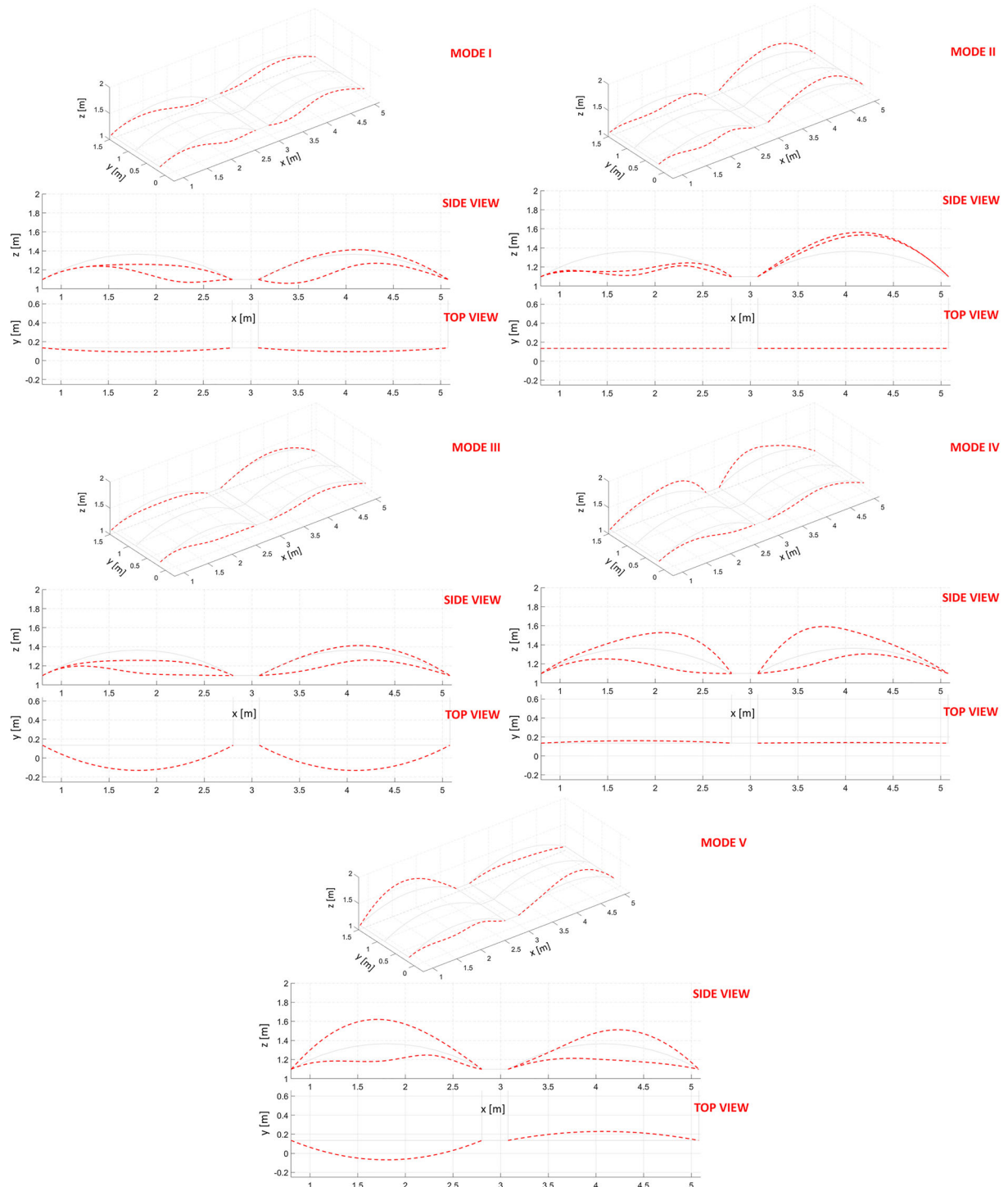
F I G U R E 8 Resulting mode shapes. The dotted red lines represent the external edges; HS.

TABLE 6 Modal assurance criterion (MAC) values between the mode shapes of Figure 8 and the known targets; HS

	Mode I	Mode II	Mode III	Mode IV	Mode V
MAC value (identified vs. target) (−)	0.9934	0.8813	0.9317	0.9415	0.8952
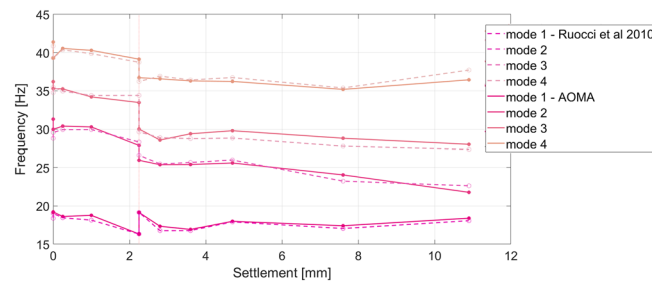
FIGURE 9 Trends of the first four natural frequencies for an increasing level of damage induced by the simulated scouring
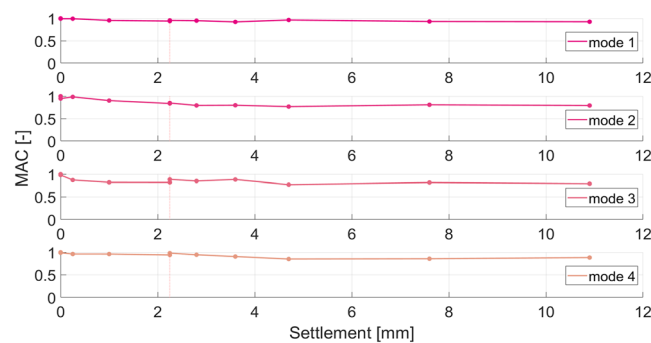
FIGURE 10 Trends of the MAC value of the first four mode shapes

On the other hand, the damping ratios were found to follow no particular trend, again similar to what was evidenced by Ruocci.[53] Indeed, it is known that, while theoretically possible,[63] the shift of modal damping alone is generally too variable to be useful as a robust damage-sensitive feature. This mainly derives from the reasons explained in the previous sections, that is to say, the high uncertainties typical of damping estimation,[45] which is also strongly affected by the sensor layout.[45]

Finally, the difference between the damaged and undamaged mode shapes can be used as well as a damage indicator, even if the magnitude changes in the measured modal vectors might be minimal.[64] This is reported in Figure 10 in terms of MAC values. In this case, the first mode showed limited degradation over the consecutive settlement steps, never falling below 92%. This decrease is more pronounced for the higher modes, reaching a minimum slightly below 80% for both the second and third modes and at about 85% for Mode 4. The mode shapes, however, seem to be less affected by the relaxation issue between the first and the second campaigns.

4.2.2 | Variability over multiple acquisitions or different sensor layouts

Figure 11 investigates the variability of the recordings by comparing the three acquisitions for the first setup. Please note that Acquisition #3 (in blue) is the one analysed in detail so far. One can notice that Acquisition #2 (in yellow) returned a spurious mode at 46.6 Hz, even considering the higher 80% confidence threshold.

Figure 12 presents a similar comparison, superposing two acquisitions taken with the two sensors setups. Please note that the signal for Setup #1 (in pink) is, again, the one discussed step by step in the previous parts of this section, i.e., the one labelled as Acquisition #3 in Figure 11.
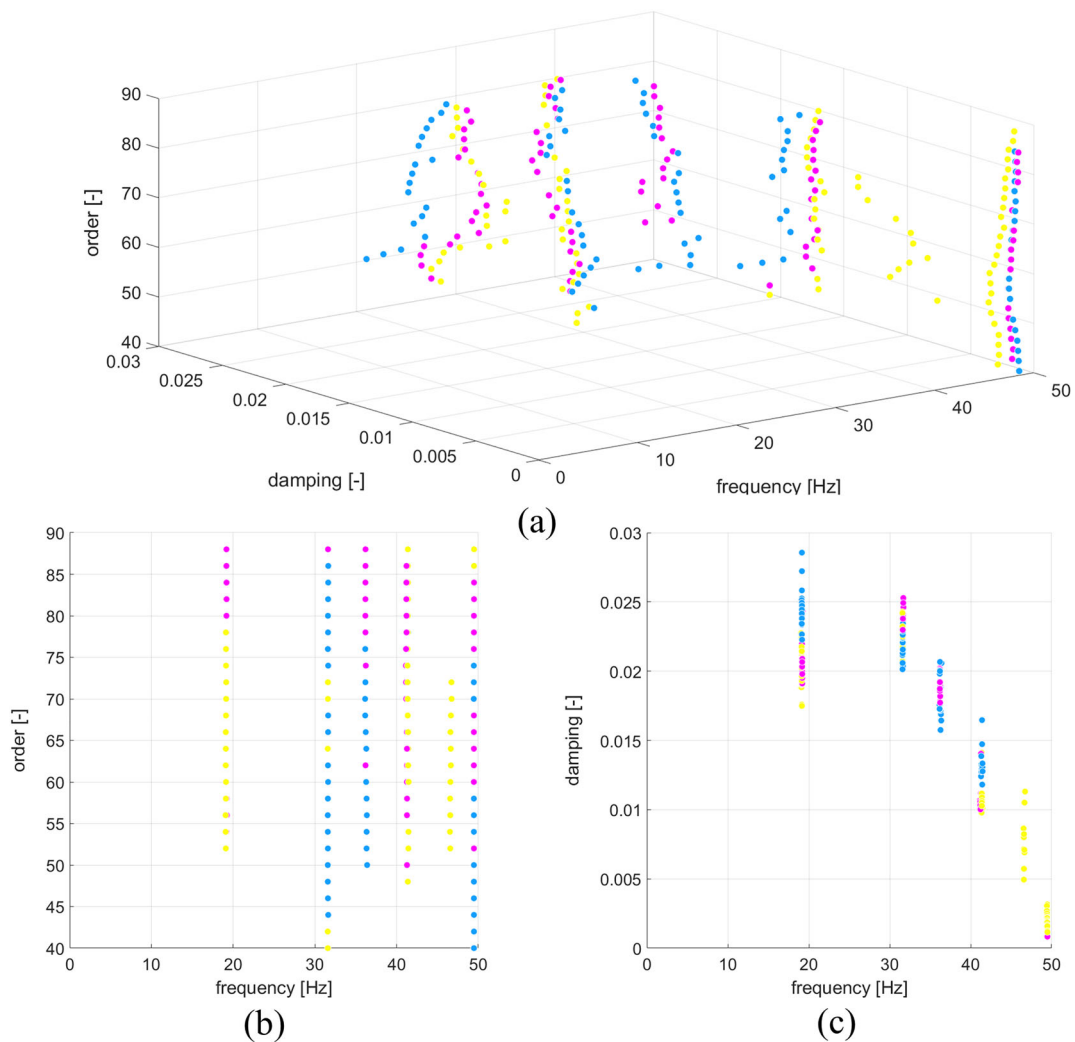
FIGURE 11 Extracted modes from three distinct AV acquisitions (Setup #1, HS). Results from Acquisition #1 in pink, Acquisition #2 in yellow, and Acquisition #3 in blue

All the recordings with the second setup were performed on 8 April 2009; the ones from the first setup on 2 April 2009. Temperature and relative humidity were checked and found to be comparable to exclude potential environmental effects[53] since they are known to be non-negligible on masonry structures.[61] Nevertheless, it can be seen that there is a large variability between the two layouts, especially regarding the estimation of the modal damping ratios. On the one hand, as anticipated above, the second returned more realistic values for the damping coefficient of the fifth vibrational mode. On the other hand, this second setup was found to struggle more to identify the third and the fourth modes, which (as it will be better explained later) were the most difficult to detect (as also discussed in Ruocci[53]).

4.2.3 | Robustness to measurement noise

The proposed algorithm performed efficiently with the noise measurement naturally included in the experimental data. However, in situ applications on real-scale structures might be affected by higher levels of noise in the acceleration records. Therefore, to further verify the robustness of the proposed algorithm, a sensitivity analysis was performed by artificially adding signal noise (assumed to be normally distributed, with zero mean and increasing standard deviation) to one signal recorded of the baseline (undamaged) structure. For comparability, Acquisition #3, seen in the previous subsection, was selected.
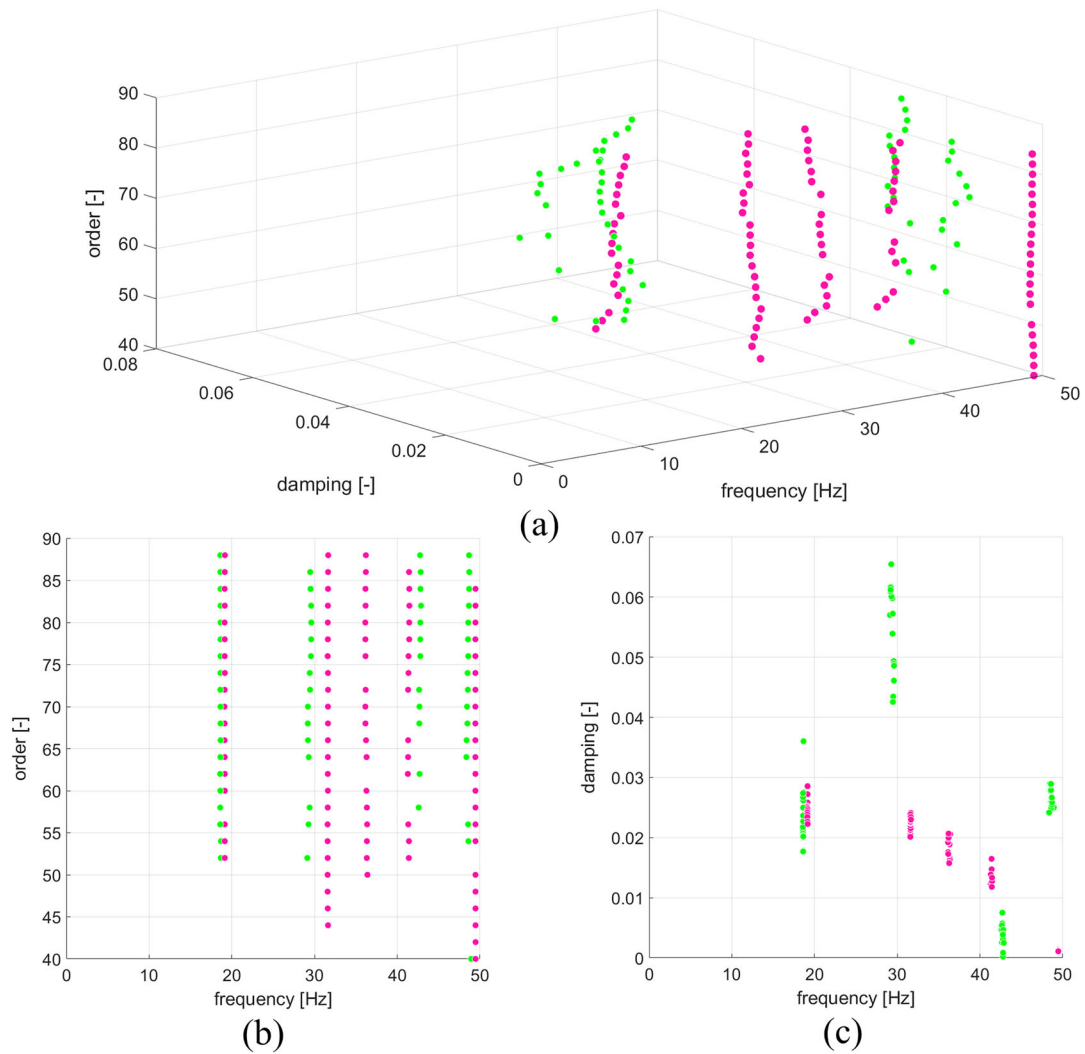
FIGURE 12 Extracted modes from the two sensor setups (HS). Results from Setup #1 in pink, Setup #2 in green. This latter layout fails to identify the third mode (first lateral bending) at circa 36 Hz.

The results reported in Table 7 refer to $\sigma_n = 0.01, 0.02, 0.05,$ and 0.10.

4.3 | Sensitivity analysis on the range of modal orders

To conclude, in previous works[42] it was highlighted the importance of the range of modal orders considered for the stabilisation diagram. Thus, a sensitivity analysis is reported here as the last study, considering the two variables n_{min} and n_{max}. These were varied between $n_{min} = 20 \div 40$ and $n_{max} = 70 \div 90$ respectively. Thus, the resulting study spanned over 121 possible n_{min}/n_{max} combinations. The resulting ranges included a minimum of 15 orders ($n_{min} = 40$ to $n_{max} = 70$) to a maximum of 35 orders ($n_{min} = 20$ to $n_{max} = 90$). Figure 13 summarises the findings of this investigation on the HS condition (Setup #1, Acquisition #3), i.e., the same dataset described previously throughout the whole Section 4.2. The semiaxes of the ellipses along the x- and y-axes represent three standard deviations (i.e., a 99.73% probability for a Gaussian distribution) around the mean natural frequency and damping ratio. It can be seen that the two spurious modes encountered before (Figure 8a,b) are still rarely found; their ellipses are marked in red. Of the remaining five physically meaningful modes, only the second one is always identified for any range of model orders. The fifth mode is almost always identified as well, missing only five times for $n_{max} = 70$. The other modes follow the distribution represented in Figure 14.

TABLE 7 The first five natural frequencies for an increasing level of artificially added measurement noise

Mode	AOMA procedure (healthy state)				
Natural frequency (Hz)					
	$\sigma_n = 0$ (noiseless)	$\sigma_n = 0.01$	$\sigma_n = 0.020$	$\sigma_n = 0.05$	$\sigma_n = 0.10$
I	19.14	19.14	19.15	—	—
II	31.61	31.60	31.59	31.61	31.64
III	36.23	36.22	34.68	—	—
IV	41.38	41.32	—	—	—
V	49.45	49.45	49.44	49.46	49.46
Damping ratio (%)					
	$\sigma_n = 0$ (noiseless)	$\sigma_n = 0.010$	$\sigma_n = 0.020$	$\sigma_n = 0.050$	$\sigma_n = 0.100$
I	2.5	2.4	2.4	—	—
II	2.2	3.4	2.3	2.7	3.3
III	1.8	2.2	1.9	—	—
IV	1.3	1.8	—	—	—
V	0.1	0.1	0.1	0.1	0.2
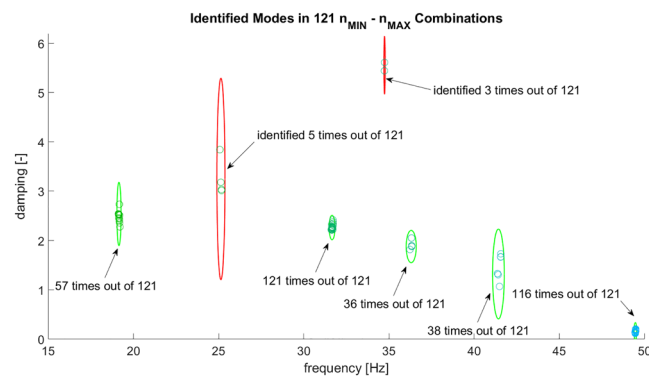
FIGURE 13 Identified modes for varying ranges of orders. The interval of confidence is coloured in red for mathematical modes and in green for the physical ones (HS, Setup #1, Acquisition #3)

Basically, the third and fourth modes are consistently found for $n_{max} > 86$ and $n_{max} > 84$ respectively, quite independently from the number of orders considered. The first mode as well can be found for almost all cases with $n_{max} > 86$, regardless of n_{min}; however, for lower values of n_{max}, it is counterintuitively easier identified for higher values of n_{min} (i.e., for shorter ranges). For unknown reasons, $n_{max} = 72$ was particularly sensitive to this specific mode. It can be seen that, on the other hand, the spurious modes appear for larger ranges, with high n_{max} and low n_{min}. Therefore, the empirical findings of this conclusive sensitivity analysis can be enlisted as follow:

- The maximum order considered, n_{max}, is the most sensitive parameter for the identification of physical modes.
- Shorter ranges, with higher values of n_{min} for high enough n_{max}, can help in stabilising the identification of some modes.
- Longer ranges not only produce more clusters but also increase the probability of labelling a computational mode as a physical one.

The main conclusion is that, for civil structures where only the lowest vibrational modes are the ones of practical interest, it is arguably more useful to use shorter ranges with high n_{max} and high n_{min} to extract only the low-frequency modes with a good probability of being physically meaningful. However, these findings may be case specific and will require further investigations over a larger experimental dataset of similar masonry arch bridges before being fully validated.
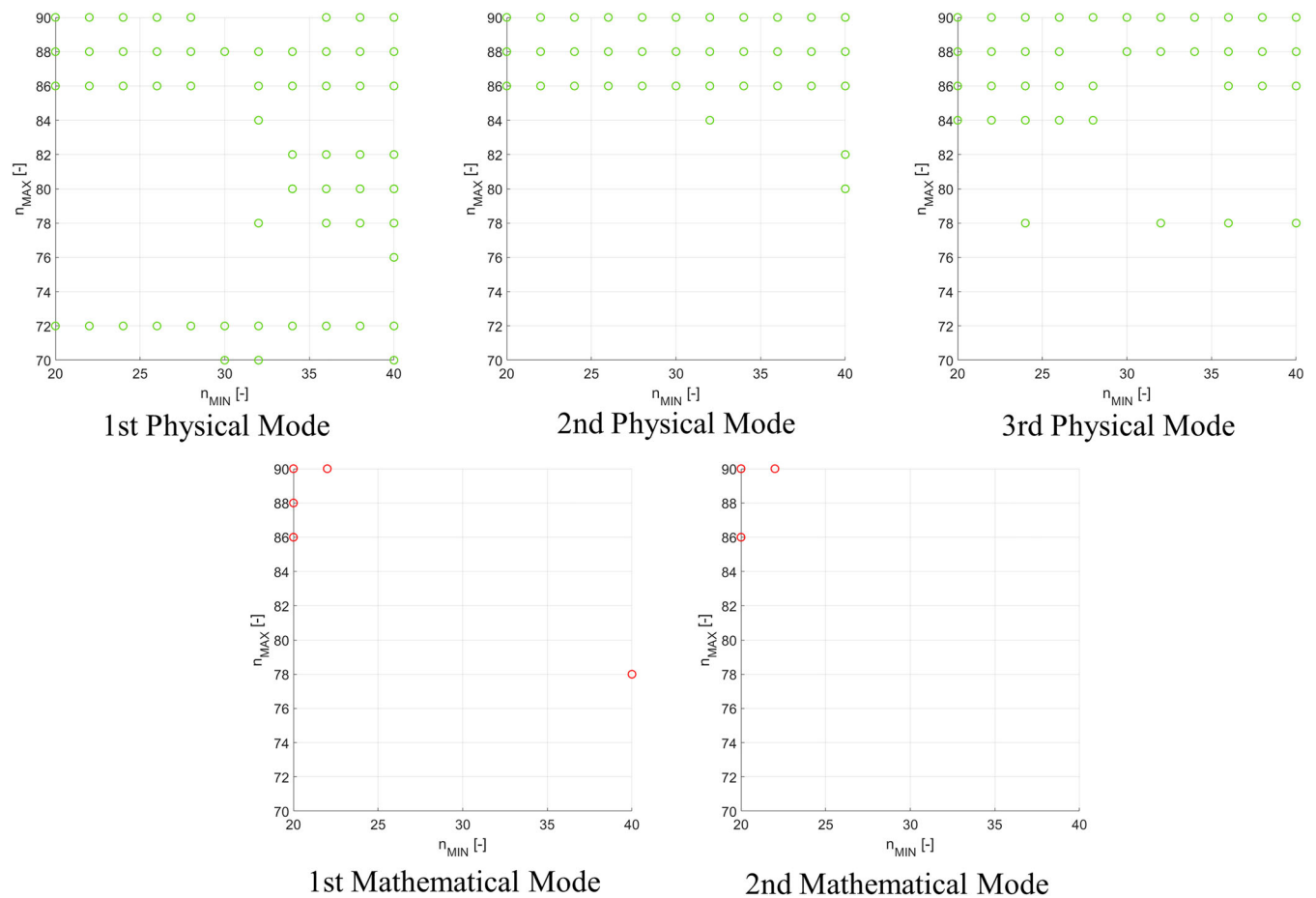
FIGURE 14 Identified modes according to the n_{min} and n_{max} values (HS)

5 | CONCLUSIONS

This paper showed how the proposed AOMA algorithm can be applied for the continuous SHM of masonry arch bridges. To the best of the authors' knowledge, this is the first experimental investigation for such application to this typology of historical infrastructures. The procedure returned the vibrational modes of a compelling experimental case study—a 1:2 scale model, subject to several steps of increasing damage. This experimental validation proves that the proposed algorithm can be reliably applied to masonry structures, especially arch bridges, for their SI and damage assessment.

Furthermore, it has been shown how the selection of physical mode by k-means clustering, commonly found in the inherent scientific literature, might be overconservative for signals with high noise levels and/or noise-like non-linear distortions. This results in mathematical (unphysical) modes still being accepted as probably physical. The variation proposed here allows to arbitrarily vary this selection criterion, making it as stricter as required. The process is statistically principled since it considers the distance between the two centroids for the 'CM' and 'PP' clusters. For the application investigated here, good results were obtained by discarding any pole closer to CM than 80% of this distance. Finally, a comprehensive investigation of the effects of varying the range of model orders was reported. Future works will be needed to validate the proposed algorithm on real-scale, in situ masonry arch bridges.

AUTHOR CONTRIBUTIONS

Marco Civera: conceptualization, methodology, software, data curation, writing – original draft, visualization and supervision. **Vezio Mugnaini:** conceptualization, methodology and software. **Luca Zanotti Fragonara:** conceptualization, methodology, data curation, writing – review & editing, supervision and project administration.

DATA AVAILABILITY STATEMENT

Data available on request from the authors.

ORCID

Marco Civera https://orcid.org/0000-0003-0414-7440
Luca Zanotti Fragonara https://orcid.org/0000-0001-6269-5280

REFERENCES

1. Farrar CR, Worden K. *Structural Health Monitoring: A Machine Learning Perspective*; 2013. doi:10.1002/9781118443118.
2. Ljung L. *System Identification*. Wiley Encycl Electr Electron Eng; 1999. doi:10.1002/047134608X.W1046.
3. Ceravolo R, Pistone G, Fragonara LZ, Massetto S, Abbiati G. Vibration-based monitoring and diagnosis of cultural heritage: a methodological discussion in three examples. *Int J Archit Herit*. 2016;10(4):375-395. doi:10.1080/15583058.2013.850554
4. Civera M, Calamai G, Fragonara LZ. Experimental modal analysis of structural systems by using the fast relaxed vector fitting method. *Struct Control Health Monit*. 2021;e2695. doi:10.1002/stc.2695
5. Civera M, Calamai G, Fragonara LZ. System identification via fast relaxed vector fitting for the structural health monitoring of masonry bridges. *Structure*. 2021;30:277-293. doi:10.1016/j.istruc.2020.12.073
6. Brincker R, Ventura CE. *Introduction to Operational Modal Analysis*. Chichester, UK: John Wiley & Sons, Ltd; 2015. doi:10.1002/9781118535141.
7. Magalhães F, Cunha Á. Explaining operational modal analysis with data from an arch bridge. *Mech Syst Signal Process*. 2011;25(5):1431-1450. doi:10.1016/j.ymssp.2010.08.001
8. Brownjohn JMW, Magalhaes F, Caetano E, Cunha A. Ambient vibration re-testing and operational modal analysis of the Humber Bridge. *Eng Struct*. 2010;32(8):2003-2018. doi:10.1016/j.engstruct.2010.02.034
9. Benedettini F, Gentile C. Operational modal testing and FE model tuning of a cable-stayed bridge. *Eng Struct*. 2011;33(6):2063-2073. doi:10.1016/j.engstruct.2011.02.046
10. Hong AL, Ubertini F, Betti R. Wind analysis of a suspension bridge: identification and finite-element model simulation. *J Struct Eng*. 2011;137(1):133-142. doi:10.1061/(ASCE)ST.1943-541X.0000279
11. Chiaia B, Marasco G, Ventura G, Quirini CZ. Customised active monitoring system for structural control and maintenance optimisation. *J Civ Struct Heal Monit*. 2019;10(2):267-282. doi:10.1007/s13349-020-00382-8
12. Peeters B, de Roeck G. Stochastic system identification for operational modal analysis: a review. *J Dyn Syst Meas Control Trans ASME*. 2001;123(4):659-667. doi:10.1115/1.1410370
13. Reynders E. System identification methods for (operational) modal analysis: review and comparison. *Arch Comput Methods Eng*. 2012;19(1):51-124. doi:10.1007/s11831-012-9069-x
14. Pecorelli ML, Ceravolo R, Epicoco R. An automatic modal identification procedure for the permanent dynamic monitoring of the sanctuary of vicoforte. *Int J Archit Herit*. 2018;14(4):630-644. doi:10.1080/15583058.2018.1554725
15. Peeters B, de Roeck G. One-year monitoring of the Z24-Bridge: environmental effects versus damage events. *Earthq Eng Struct Dyn*. 2001;30(2):149-171.
16. Cross EJ, Koo KY, Brownjohn JMW, Worden K. Long-term monitoring and data analysis of the Tamar Bridge. *Mech Syst Signal Process*. 2013;35(1–2):16-34. doi:10.1016/j.ymssp.2012.08.026
17. Rainieri C, Fabbrocino G. Automated output-only dynamic identification of civil engineering structures. *Mech Syst Signal Process*. 2010;24(3):678-695. doi:10.1016/j.ymssp.2009.10.003
18. Cheema P, Alamdari MM, Vio GA, Zhang FL, Kim CW. Infinite mixture models for operational modal analysis: an automated and principled approach. *J Sound Vib*. 2021;491:115757. doi:10.1016/J.JSV.2020.115757
19. He M, Liang P, Li J, Zhang Y, Liu Y. Fully automated precise operational modal identification. *Eng Struct*. 2021;234:111988. doi:10.1016/J.ENGSTRUCT.2021.111988
20. Zeng J, Hoon Kim Y. A two-stage framework for automated operational modal identification. *Struct Infrastruct Eng*. 2021;1-20. doi:10.1080/15732479.2021.1919151
21. Anastasopoulos D, de Roeck G, Reynders EPB. One-year operational modal analysis of a steel bridge from high-resolution macrostrain monitoring: influence of temperature vs. retrofitting. *Mech Syst Signal Process*. 2021;161:107951. doi:10.1016/J.YMSSP.2021.107951
22. Reynders E, Schevenels M, Roeck G. MACEC 3.3 a Matlab toolbox for experimental and operational modal analysis. 2014.
23. Peeters B, de Roeck G. Reference-based stochastic subspace identification for output-only modal analysis. *Mech Syst Signal Process*. 1999;13(6):855-878. doi:10.1006/mssp.1999.1249
24. Reynders E, Degrauwe D, de Roeck G, Magalhães F, Caetano E. Combined experimental-operational modal testing of footbridges. *J Eng Mech*. 2010;136(6):687-696. doi:10.1061/(ASCE)EM.1943-7889.0000119

25. Reynders E, de Roeck G, Gundes Bakir P, Sauvage C. Damage identification on the Tilff Bridge by vibration monitoring using optical fiber strain sensors. *J Eng Mech*. 2007;133(2):185-193. doi:10.1061/(ASCE)0733-9399(2007)133:2(185

26. Liu K, Reynders E, de Roeck G, Lombaert G. Experimental and numerical analysis of a composite bridge for high-speed trains. *J Sound Vib*. 2009;320(1–2):201-220. doi:10.1016/j.jsv.2008.07.010

27. Lourenço PB. Computations on historic masonry structures. *Prog Struct Eng Mater*. 2002;4(3):301-319. doi:10.1002/pse.120

28. Lourenço PB. *Structural Masonry Analysis: Recent Developments and Prospects*. Australia: University of Newcastle; 2008.

29. Civera M, Pecorelli ML, Ceravolo R, Surace C, Fragonara LZ. A multi-objective genetic algorithm strategy for robust optimal sensor placement. *Comput Civ Infrastruct Eng*. 2021;36(9):1185-1202. doi:10.1111/mice.12646

30. Marmolejo MA, Marulanda J, Miraglia G, Thomson P, Ceravolo R. Time-frequency domain identification of modal parameters in complex masonry structures under ambient vibrations. *Procedia Eng*. 2017;199:2184-2189. doi:10.1016/j.proeng.2017.09.178

31. Scozzese F, Ragni L, Tubaldi E, Gara F. Modal properties variation and collapse assessment of masonry arch bridges under scour action. *Eng Struct*. 2019;199:109665. doi:10.1016/j.engstruct.2019.109665

32. Costa C, Ribeiro D, Jorge P, Silva R, Calçada R, Arêde A. Calibration of the numerical model of a short-span masonry railway bridge based on experimental modal parameters. *Procedia Eng*. 2015;114:846-853. doi:10.1016/J.PROENG.2015.08.038

33. Costa C, Ribeiro D, Jorge P, Silva R, Arêde A, Calçada R. Calibration of the numerical model of a stone masonry railway bridge based on experimentally identified modal parameters. *Eng Struct C*. 2016;123:354-371. doi:10.1016/J.ENGSTRUCT.2016.05.044

34. Deraemaeker A, Reynders E, de Roeck G, Kullaa J. Vibration-based structural health monitoring using output-only measurements under changing environment. *Mech Syst Signal Process*. 2008;22(1):34-56. doi:10.1016/j.ymssp.2007.07.004

35. Reynders E, de Roeck G. Continuous vibration monitoring and progressive damage testing on the Z24 bridge. In: *Encyclopedia of Structural Health Monitoring*. Chichester, UK: John Wiley & Sons, Ltd; 2008.

36. Reynders E, de Roeck G. Vibration-based damage identification: the Z24 bridge benchmark. *Encycl Earthq Eng*. 2015; doi:10.1007/978-3-642-35344-4_72

37. Mao J-X, Wang H, Fu Y-G, Spencer BF. Automated modal identification using principal component and cluster analysis: application to a long-span cable-stayed bridge. *Struct Control Health Monit*. 2019;26(10):e2430. doi:10.1002/STC.2430

38. Cabboi A, Magalhães F, Gentile C, Cunha Á. Automated modal identification and tracking: application to an iron arch bridge. *Struct Control Health Monit*. 2017;24(1):e1854. doi:10.1002/stc.1854

39. Fan G, Li J, Hao H. Improved automated operational modal identification of structures based on clustering. *Struct Control Health Monit*. 2019;26(12):e2450. doi:10.1002/STC.2450

40. Reynders E, Houbrechts J, de Roeck G. Fully automated (operational) modal analysis. *Mech Syst Signal Process*. 2012;29:228-250. doi:10.1016/j.ymssp.2012.01.007

41. Demarie GV, Sabia D. A machine learning approach for the automatic long-term structural health monitoring. *Struct Heal Monit*. 2019;18(3):819-837. doi:10.1177/1475921718779193

42. Mugnaini V, Fragonara LZ, Civera M. A machine learning approach for automatic operational modal analysis. *Mech Syst Signal Process*. 2022;170:108813. doi:10.1016/j.ymssp.2022.108813

43. Allemang RJ, Brown DL. A correlation coefficient for modal vector analysis. In: Proceedings of the 1st International Modal Analysis Conference (IMAC 1982). 1982; 110-116.

44. Phillips AW, Allemang RJ. Application of modal scaling to the pole selection phase of parameter estimation. *Struct Dyn*. 2011;3:499-518.

45. Reynders E, Pintelon R, de Roeck G. Uncertainty bounds on modal parameters obtained from stochastic subspace identification. *Mech Syst Signal Process*. 2008;22(4):948-969. doi:10.1016/j.ymssp.2007.10.009

46. Lloyd SP. Least squares quantization in PCM. *IEEE Trans Inf Theory*. 1982;28(2):1982-1137. doi:10.1109/TIT.1982.1056489

47. Neu E, Janser F, Khatibi AA, Orifici AC. Fully automated operational modal analysis using multi-stage clustering. *Mech Syst Signal Process*. 2017;84:308-323. doi:10.1016/j.ymssp.2016.07.031

48. Box GEP, Cox DR. An analysis of transformations. *J R Stat Soc Ser B*. 1964;26(2):211-243. doi:10.1111/j.2517-6161.1964.tb00553.x

49. Seifoddini HK. Single linkage versus average linkage clustering in machine cells formation applications. *Comput Ind Eng*. 1989;16(3):419-426. doi:10.1016/0360-8352(89)90160-5

50. Aggarwal CC. *Data Mining: The Textbook*. Springer New York; 2015. doi:10.1007/978-3-319-14142-8.

51. Mosteller F, Tukey JW. Data analysis and regression: a second course in statistics. 1977.

52. Ruocci G, Degiovanni L, Quattrone A, Fragonara LZ, Ceravolo R, de Stefano A. Experimental testing of a masonry arch bridge model subject to increasing level of damage. 2011. European Commission.

53. Ruocci G. Application of the SHM methodologies to the protection of masonry arch bridges from scour. 2010.

54. Ruocci G, Ceravolo R, de Stefano A. Modal identification of an experimental model of masonry arch bridge. *Key Eng Mater*. 2009;413–414:707-714. doi:10.4028/www.scientific.net/KEM.413-414.707

55. Zanotti Fragonara L, Ceravolo R, Matta E, Quattrone A, de Stefano A, Pecorelli M. Non-linear characterisation of the physical model of an ancient masonry bridge. In: J Phys Conf Ser. Institute of Physics Publishing, 2012; 012051.

56. van Overschee P, de Moor B. *Subspace Identification for Linear Systems*. Springer US; 1996. doi:10.1007/978-1-4613-0465-4.

57. Aranganayagi S, Thangavel K. Clustering categorical data using silhouette coefficient as a relocating measure. In: International Conference on Computational Intelligence and Multimedia Applications (ICCIMA 2007). 2007.

58. Oh CK, Sohn H. Damage diagnosis under environmental and operational variations using unsupervised support vector machine. *J Sound Vib*. 2009;325(1-2):224-239. doi:10.1016/j.jsv.2009.03.014

59. Cross EJ, Manson G, Worden K, Pierce SG. Features for damage detection with insensitivity to environmental and operational variations. *Proc R Soc a Math Phys Eng Sci.* 2012;468(2148):4098-4122. doi:10.1098/rspa.2012.0031

60. Limongelli MP. Frequency response function interpolation for damage detection under changing environment. *Mech Syst Signal Process.* 2010;24(8):2898-2913. doi:10.1016/J.YMSSP.2010.03.004

61. Ceravolo R, de Lucia G, Miraglia G, Pecorelli ML. Thermoelastic finite element model updating with application to monumental buildings. *Comput Civ Infrastruct Eng.* 2020;35(6):628-642. doi:10.1111/mice.12516

62. Sohn H. Effects of environmental and operational variability on structural health monitoring. *Philos Trans R Soc a Math Phys Eng Sci.* 2007;365(1851):539-560. doi:10.1098/rsta.2006.1935

63. Curadelli RO, Riera JD, Ambrosini D, Amani MG. Damage detection by means of structural damping identification. *Eng Struct.* 2008; 30(12):3497-3504. doi:10.1016/j.engstruct.2008.05.024

64. Allemang RJJ. The modal assurance criterion—twenty years of use and abuse. *Sound Vib.* 2003;1(3-4):14-21. doi:10.1016/j.chemgeo. 2006.02.014